AD-A259 979

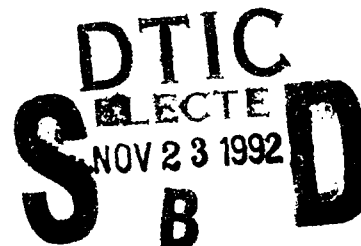# DAMAGE PROCESSES IN A QUASI-ISOTROPIC COMPOSITE SHORT BEAM UNDER THREE-POINT LOADING

Bryan H. Fortson and Erian A. Armanios

September 1992

Journal Article

DTIC
SELECTED
NOV 23 1992
B

92-30032

PL-TR--92-1015

This final report was prepared by the Phillips Laboratory, Kirtland Air Force Base, New Mexico, under Job Order 9993LABS. The Phillips Laboratory Project Officer-in-Charge was Capt. Bryan H. Fortson (WSSD).

This report has been reviewed and is approved for publication.

Bryan H. Fortson, Capt. USAF
Project Officer

FOR THE COMMANDER

Firooz A. Allahdadi, GM-14
Chief, Space Kinetic Impact &
Debris Branch

Brendan B. Godfrey, Acting Director
Advanced Weapons & Survivability
Directorate

REPORT DOCUMENTATION PAGE

Public reporting burden for this collection of information is estimated to average 1 hour per response, including the time for reviewing instructions, searching existing data sources, gathering and maintaining the data needed, and completing and reviewing the collection of information. Send comments regarding this burden estimate or any other aspect of this collection of information, including suggestions for reducing this burden, to Washington Headquarters Services, Directorate for Information Operations and Reports, 1215 Jefferson Davis Highway, Suite 1204, Arlington, VA 22202-4302, and to the Office of Management and Budget, Paperwork Reduction Project (0704-0188), Washington, DC 20503

1. AGENCY USE ONLY (Leave blank)	2. REPORT DATE September 1992	3. REPORT TYPE AND DATES COVERED Journal Article

4. TITLE AND SUBTITLE	5. FUNDING NUMBERS
DAMAGE PROCESSES IN A QUASI-ISOTROPIC COMPOSITE SHORT BEAM UNDER THREE-POINT LOADING	PR: 9993 TA: LA WU: BS

6. AUTHOR(S)

Bryan H. Fortson and Erian A. Armanios

7. PERFORMING ORGANIZATION NAME(S) AND ADDRESS(ES)	8. PERFORMING ORGANIZATION REPORT NUMBER

9. SPONSORING / MONITORING AGENCY NAME(S) AND ADDRESS(ES)	10. SPONSORING / MONITORING AGENCY REPORT NUMBER
Space Kinetic Impact and Debris Branch Space Survivability Division Advanced Weapons and Survivability Directorate Phillips Laboratory Kirtland AFB, NM 87117-6008	PL TR-92-1043

11. SUPPLEMENTARY NOTES

12a. DISTRIBUTION / AVAILABILITY STATEMENT	12b. DISTRIBUTION CODE
Approved for public release; distribution is unlimited.	

13. ABSTRACT (Maximum 200 words)

Composite materials have complex failure modes that include delamination, fiber debonding and breakage, and matrix microcracking. In this paper, the influence of these damage modes on the failure of the short-beam three-point bend test is investigated for a composite with a quasi-isotropic layup. Failure is found to initiate in a region near the point of application of the load, a location where classical-type analytical descriptions of specimen behavior are unreliable. Futhermore, the locations of failure show little reproducibility. Observed fracture behavior is explained in terms of the overall stress state of the beam before fracture, and failure is predicted from the stress map, using the maximum strain criterion.

14. SUBJECT TERMS			15. NUMBER OF PAGES 8
composites, delamination, fractography, finite element analysis, failure analysis			16. PRICE CODE

17. SECURITY CLASSIFICATION OF REPORT	18. SECURITY CLASSIFICATION OF THIS PAGE	19. SECURITY CLASSIFICATION OF ABSTRACT	20. LIMITATION OF ABSTRACT
Unclassified	Unclassified	Unclassified	SAR

Bryan H. Fortson[1] and Erian A. Armanios[2]

Damage Processes in a Quasi-Isotropic Composite Short Beam Under Three-Point Loading

ABSTRACT: Composite materials have complex failure modes that include delamination, fiber debonding and breakage, and matrix microcracking. In this paper, the influence of these damage modes on the failure of the short-beam three-point bend test is investigated for a composite with a quasi-isotropic layup. Failure is found to initiate in a region near the point of application of the load, a location where classical-type analytical descriptions of specimen behavior are unreliable. Furthermore, the locations of failure show little reproducibility. Observed fracture behavior is explained in terms of the overall stress state in the beam before fracture, and failure is predicted from the stress map, using the maximum strain criterion.

KEY WORDS: composites, delamination, fractography, finite element analysis, failure analysis

The three-point short-beam bending test (ASTM Test for Apparent Interlaminar Shear Strength of Parallel Fiber Composites by Short-Beam Method D 2344), as shown in Fig. 1, has long been used to quantify the shear strength of laminated composite materials. The interlaminar shear stress at failure is then calculated using the equation

$$\tau_I = \frac{3P}{4A} \qquad (1)$$

where

τ_I = interlaminar shear stress,
P = applied load at failure, and
A = cross-sectional area of the specimen.

The standard procedure for the short-beam shear test is intended for use with unidirectional composites with fibers oriented along the length of the specimen. Equation 1 is based on a parabolic through-the-thickness shear stress distribution with a maximum at the beam midplane. This simple strength of materials analysis neglects the effects of stress concentrations and material anisotropy.

[1]Formerly, graduate research assistant, School of Aerospace Engineering, Georgia Institute of Technology, Atlanta, GA; presently, simulation engineer, Space Kinetic Impact and Debris Branch, Phillips Laboratory, Kirktland Air Force Base, NM 87109.
[2]Associate professor, School of Aerospace Engineering, Georgia Institute of Technology, Atlanta, GA 30332-0150.

This test is frequently used to screen materials based on their interlaminar shear strength. However, there is concern that use of the test relies upon incorrect assumptions concerning the nature of the failure process.

Whitney and Browning, in Ref 1, in examining the failure of unidirectional short-beam specimens, discovered that pure Mode II failure along the specimen midplane was not the mode of fracture. Rather, compressive stresses in the regions of high interlaminar shear stress were found to suppress interlaminar-shear failure modes, and initial damage as a result of vertical cracking was found to precede final failure caused by large-scale delamination. If the failure process is this complex, then the applied load at failure does not depend solely on the interlaminar shear strength, making the test useless for its intended purpose.

The elastoplastic finite element analysis of Berg et al. [2] showed extremely high shear stresses near the load nose, and the finite difference analysis of Sandorff [3] showed that St. Venant's principle is not satisfied in an orthotropic beam of low span-to-depth ratio, with the result that the stress concentration effects near the load nose and the supports are never dissipated.

Because of this uncertainty, there is a need for reexamination of the short-beam three-point bend specimen for specific composite configurations. Such an examination must determine whether a simple relationship between loading and fracture exists, and if not, what fracture processes are taking place. The current effort answers these questions for a graphite/epoxy laminate with a quasi-isotropic layup.
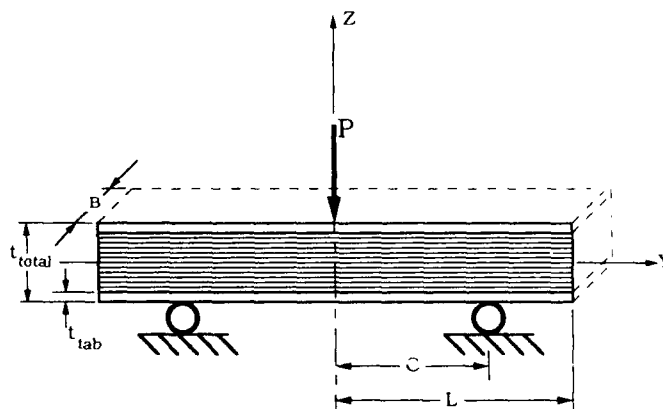

FIG. 1—*The three-point short-beam test.*

General Failure Analysis

Specimen Design and Testing

The subject of the investigation was a short-beam specimen with dimensions given in Table 1. A sample panel was fabricated and inspected for quality, using standard aerospace industry practice, before sectioning into specimens. Two fiberglass plies, each of thickness 0.457 mm (0.018 in.), were bonded to the upper and lower surfaces to minimize the bearing effect at the supports and the applied load location.

The material properties for the graphite/epoxy and the fiberglass plies are given in Table 2. The material was an AS4/3502 graphite/epoxy system, and the layup was $[\mp 45/0/90]_{n_x}$. Failure load data for four specimens tested to failure in three-point bending are given in Table 3. The shear strength predictions in the table are based on Eq 1. The failed specimens were sectioned with a silicon carbide saw, and the sections were analyzed using a scanning electron microscope (SEM).

Numerical Methods

Numerical analysis of the specimen concentrated on the phenomenon of delamination. Delamination analysis can be based on two approaches: the strain energy release rate approach and the interlaminar stress approach. The interlaminar stresses develop at interfaces between plies to keep the laminate in a state of equilibrium and kinematic compatibility. Delamination occurs when these stresses reach the interlaminar strength of the material. The strain energy release rate approach is based on the actual process of fracture, rather than the strength concept. Delamination can propagate when the strain energy release rate at

the crack front is sufficient to overcome the material's fracture resistance or toughness.

Finite-element method (FEM) analysis of the specimen was performed using two codes: Engineering Analysis Language (EAL), a linear code, and Geometrically and Materially Nonlinear Analysis of Structures (GAMNAS), a NASA-developed code described in Ref 4. Both codes were run using meshes consisting entirely of four-noded, rectangular elements, using a two-dimensional (2-D) plane-stress model. Both meshes considered one ply to be one element thick. The EAL mesh used elements of aspect ratio 5:1, except within five-ply thicknesses of the load nose and support, where the ratio was 1:1. These ratios were not the same in the fiberglass plies, which were also one element thick but had a greater real thickness than the other plies. The EAL mesh modelled only one half of the specimen, taking advantage of the symmetry of the problem about the loading axis. Figure 2 shows the mesh used for the EAL model. The number of elements is 1900, and the total number of degrees of freedom is 3940. The heavy horizontal line in the figure corresponds to an assumed crack.

Subsequent EAL models involving assumed cracks in the specimen near the free end also had mesh refinement to an aspect ratio of 1:1 in the vicinity of the crack tip. These models were used to find the strain energy release rates associated with the assumed cracks using the zero-length element method outlined in Ref 5.

TABLE 1—Dimensions of quasi-isotropic short-beam specimen, mm (in.) (see Fig. 1 for nomenclature).

L	24.40 (1.00)
c	15.875 (0.625)
t_{tab}	0.457 (0.018)
t_{total}	7.188 (0.283)
B	9.525 (0.375)

TABLE 2—Properties of specimen constituent materials.

Constant	AS4/3502	Fiberglass
E_{11}	141.34 GPa (20.50 Msi)	21.99 GPa (3.19 Msi)
$E_{22} = E_{33}$	11.51 GPa (1.67 Msi)	21.99 GPa (3.19 Msi)
$G_{12} = G_{13}$	6.00 GPa (0.87 Msi)	3.93 GPa (0.57 Msi)
G_{23}	3.45 GPa (0.50 Msi)	2.96 GPa (0.43 Msi)
$\nu_{12} = \nu_{13}$	0.26	0.11
ν_{23}	0.43	0.42

TABLE 3—Failure loads of quasi-isotropic short-beam specimens.

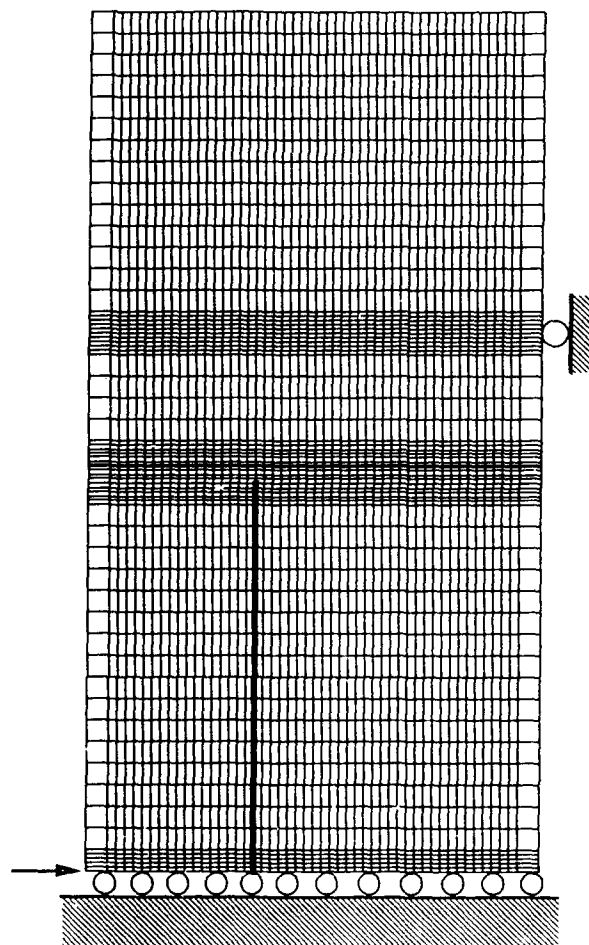| Test	Load	Shear Strength
1	4559 N (1025 lbs)	47091 kPa (6830 psi)
2	4982 N (1120 lbs)	55820 kPa (8096 psi)
3	4693 N (1055 lbs)	46560 kPa (6753 psi)
4	5894 N (1325 lbs)	53090 kPa (7700 psi)

FIG. 2—Schematic of the EAL mesh.

The GAMNAS model did not use a symmetry plane, and all elements were of approximate aspect ratio 4:1, except for elements in the fiberglass plies, which were of approximate aspect ratio 1.2:1. There are 2600 elements and 5404 degrees of freedom in this mesh. The mesh is coarse in comparison with the EAL discretization, since the element is based upon a nonlinear formulation.

The GAMNAS model was used to predict the stress field in the specimen using an assumption of geometric nonlinearity. The EAL model was used to predict the strain energy release rate using the zero-length element, as well as the stress field. Comparison of the stress field results from the two codes showed geometric nonlinearity effects to be negligible. This supports the use of the linear EAL model, which was much simpler to use for a large number of similar but nonidentical configurations.

Results of Numerical Analysis

Stress Maps—Table 4 shows the locations of delamination failure observed visually by the naked eye and using an optical microscope at ×30 magnification for a representative group of samples. Figure 3 shows the ply- and interface-numbering scheme. The table lists, for each interface, the number of specimens in
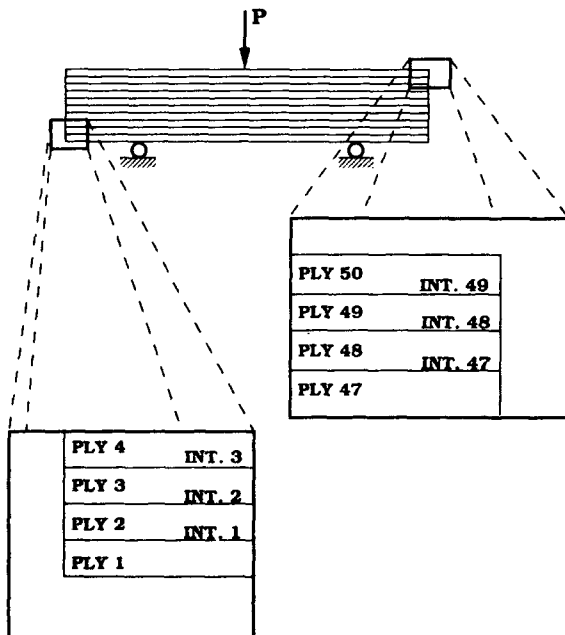
which final failure was observed for that interface. Since the layup includes 50 plies, there are 49 interfaces, of which Interface 25 is the midplane. It is seen that the failures took place well away from the midplane. Note the large amount of variation in the locations of delamination. No single interface accounts for even a majority of the observed failures. This would not be the case if fracture was driven by a simple mechanical process. In other materials, such variation in fracture behavior might be attributed to the random distribution of material defects. Several types of processing defects, such as voids, resin-rich areas, and bridged fibers, can affect fracture behavior. However, such defects usually do not drive fracture behavior to the extent found in Table 4. Also note that several specimens showed additional, secondary cracking above the midplane, indicating a complex failure process. It was observed that the delaminations did not extend for the full length of the specimen. Finally, note that all of the specimens in which one primary delamination appeared to the naked eye had that single delamination below the midplane. Figure 4 shows actual failed specimens, illustrating the variability in crack location. The locations of the roller supports and applied load are shown schematically in Fig. 5.
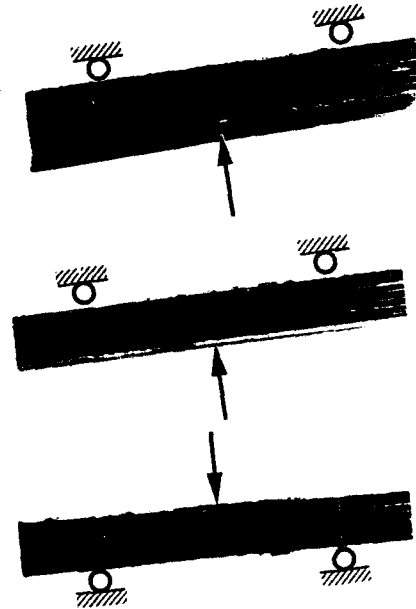
TABLE 4—*Locations of failure of short-beam specimens.*

Location, Interface No.	Number of Failures
14	5
11	2
7	2
6	2
12	1

FIG. 4—*Failed short beam specimens.*

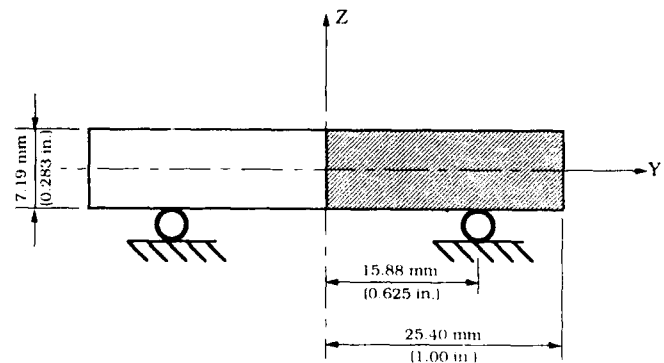FIG. 3—*Ply and interface numbering.*

FIG. 5—*Plotted region for stress and strain maps.*

The GAMNAS analysis yielded stress profiles for the specimen under load, which are shown as Figs. 6, 7, and 8. On the basis of the data shown in Table 3, a load of 4448 N (1000 lbs) was selected for these calculations. These figures show one half of the y-z plane. The coordinate system can be understood in terms of Fig. 1, which also shows the y-z plane. The origin of the coordinate system is at the midplane directly beneath the load nose. Thus, the load is applied at the point $(0, t_{total}/2)$, and the supports are located at the points $(\pm c, -t_{total}/2)$. A schematic representation of this region is shown in Fig. 5.

Figure 6 maps the peel stress σ_{zz}. The figure shows high values of compressive stress near the load nose and the support and relatively small values of peel stress elsewhere.
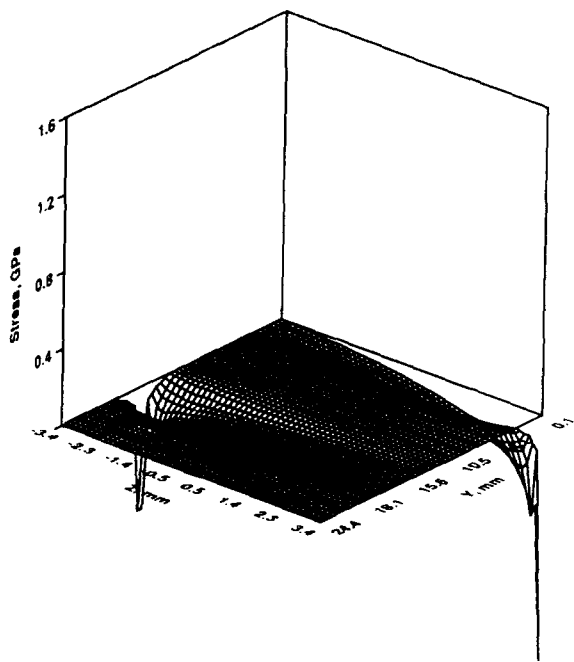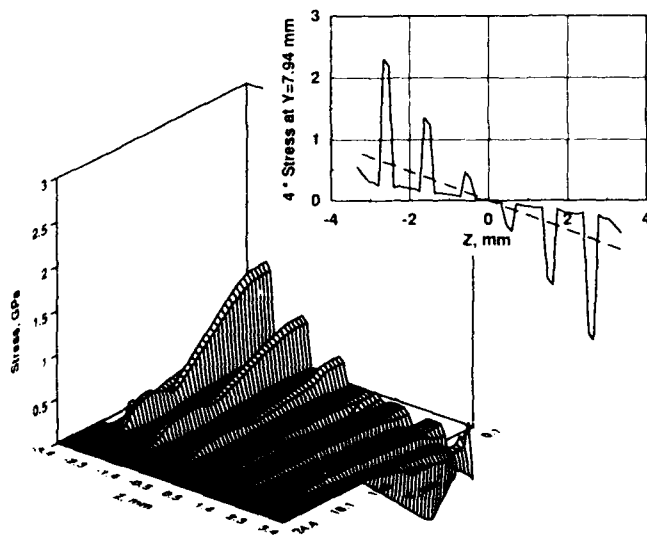
Figure 7 maps the chordwise stress σ_{yy}. This figure is much as would be expected, with a typical bending-stress profile and the largest magnitudes near the load nose. As a check for reasonableness, a two-dimensional plot of σ_{yy} appears on the insert to Fig. 7. These values are taken at $y = 7.9375$ mm (0.3125 in.), a location well removed from the stress concentrations at the load nose and support, and are shown as the light line on the plot. The dashed line graphs the σ_{yy} values predicted from isotropic beam theory for a homogeneous beam with smeared properties. This simple model well represents the magnitude and trend of the finite element data, as it should.

The map of the shear stress σ_{yz}, shown in Fig. 8, is the most significant. Major deviations from the parabolic stress profile expected from beam theory are seen. High values of shear stress are found near the load nose and support. The maximum stress values between the load nose and support are consistent with the predictions of beam theory. This is shown by an insert plot similar to that of Fig. 7.

In summary, the beam-theory analysis used to derive Eq 1 significantly underestimates the magnitude of the stress beneath the load nose and near the support, while adequately predicting it elsewhere.

Failure Predictions—Figures 6, 7, and 8 indicate that it is unlikely that damage initiates at the specimen free ends, which are nearly stress free. To confirm this, failure of the specimen was analyzed, using the maximum-strain criterion. Stress data from each element in the GAMNAS model were converted to strain data, and these strains were compared to the material strain to failure. The strains to failure for the fiber, matrix, and shear orientations are 11 100, 6800, and 20 000 $\mu\varepsilon$, respectively. The fraction of the critical strain in the fiber, matrix, and shear orientations was calculated, and the largest of these was selected, with the assigned data values capped at 100% of strain to failure. The resulting data provide a map of nearness to failure at each location in the specimen and are shown in Fig. 9. The load used for this figure is 5338 N (1200 lbs). This is similar to the actual failure loads.
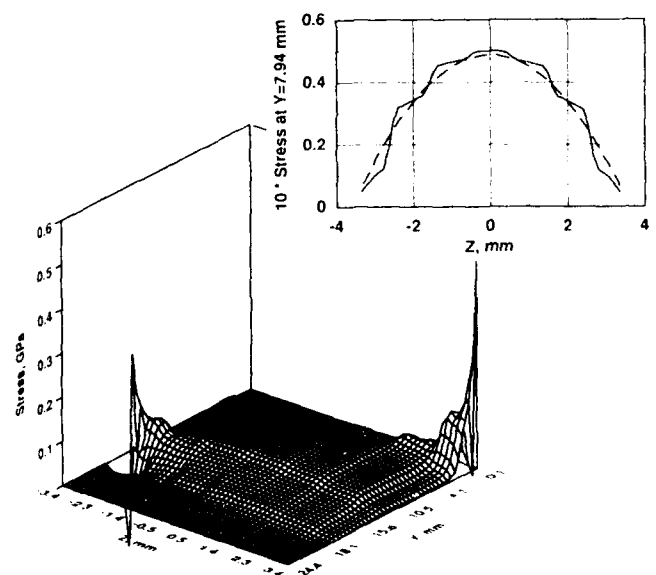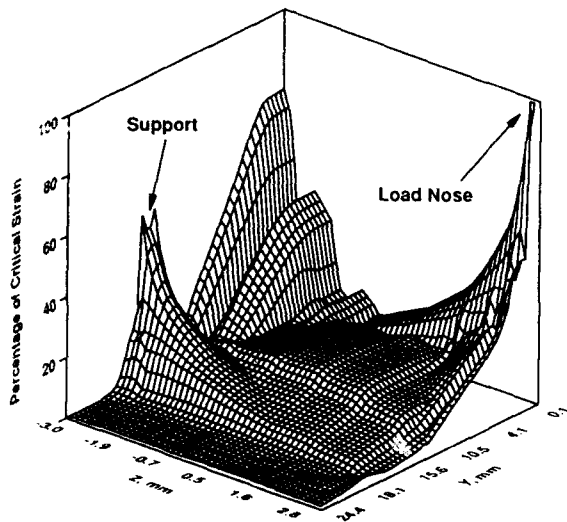

FIG. 6—Map of peel stress.

FIG. 7—Map of chordwise stress.

FIG. 8—Map of shear stress.

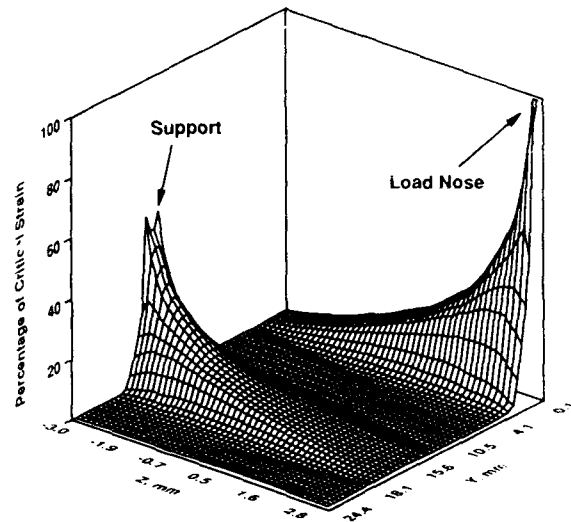FIG. 9—*Map of maximum fraction of critical strain*

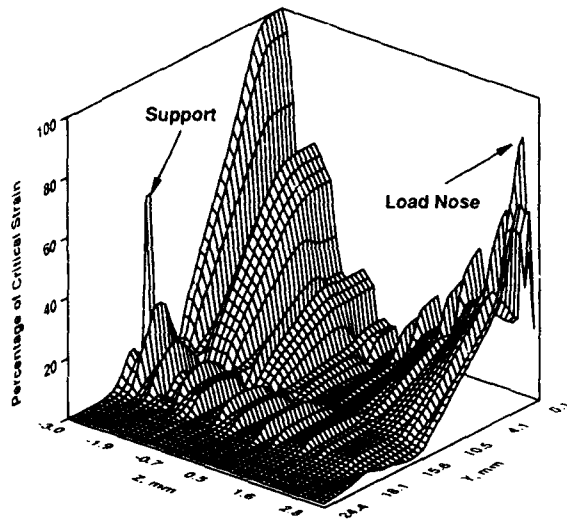FIG. 11—*Map of fraction of critical strain as a result of peel stress*

FIG. 10—*Map of fraction of critical strain as a result of chordwise stresses.*
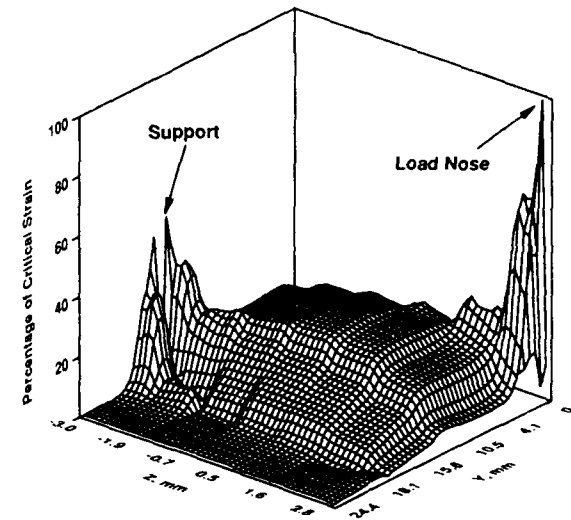

FIG. 12—*Map of fraction of critical strain as a result of shear stresses.*

Figures 10, 11, and 12 show nearness to failure maps for the three stress components: chordwise, peel, and shear. Considered along with Fig. 9, they offer insights into the possible causes of failure at various locations. For example, Fig. 9 shows that failure is imminent in the region near the load nose; reference to Figs. 10, 11, and 12 shows that this is primarily due to chordwise stresses, although peel and shear stresses could also contribute. Failure as a result of crushing is also incipient near the support, and failure as a result of chordwise stresses below the midplane near the load nose is also a possibility. In contrast, the midplane, where beam theory predicts the largest shear stresses, is the region least vulnerable to failure. This is consistent with the observed cracks in the tested specimens, which failed below the midplane and sometimes above it, but never on or near the midplane.

The maximum strain-to-failure map of Fig. 9 was modified to include additional failure modes observed by McCleskey[3] for laminates made of glass-epoxy material. McCleskey's laminates consisted of eight plies, each of thickness 0.8255 mm (0.0325 in.), and were of layup [90/ − 45/45/0]$_s$. When these specimens were tested in three-point bending, a 0° ply near the midplane was observed to crack at an angle of 45° to the midplane, as shown in Fig. 13. McCleskey suggested that these failures were due to the state of nearly pure shear near the specimen midplane resolving itself into a tensile stress at a 45° angle to the midplane. This stress would act upon the matrix of a 0° ply.

[3]S. F. McCleskey, private communication, 31st AIAA ASME ASCE AHS/ASC Structures, Structural Dynamics and Materials Conference. Long Beach, CA. 2–4 April 1990.

This effect could be modelled as shown in Fig. 14. It is assumed that any normal stress in the y-z plane leads to matrix-driven failure in a 0° ply. Thus, to determine the maximum effect of normal stresses upon such a ply, it is necessary to determine the largest normal stress operating in the y-z plane; if σ_{xx} is assumed to be zero, then this largest normal stress is the principal stress with the largest magnitude. The percentage of strain to failure can then be calculated using this largest principal stress, and the appropriate tensile or compressive modulus for loads applied normal to the fibers.

A similar phenomenon might take place in the 45° plies, leading to a failure surface as shown in Fig. 15. To predict this second additional failure mode, it would be necessary to determine the traction normal to the fracture surface shown in this figure, and therefore, to perform a three-dimensional stress transformation, assuming the out-of-plane stresses to be zero. The percentage of strain to failure for this fracture mode could then be calculated using the traction resolved on this face, and the appropriate tensile or compressive modulus for loads applied normal to the fibers.

The analysis that produced Fig. 9 was modified to include the two additional failure modes and was repeated, with results as shown in Figs. 16, 17, and 18. The areas in which Figs. 9 and 16 differ are, therefore, areas in which one of the McCleskey failure modes determines fracture. Comparison of Figs. 9 and 16 shows one change as a result of these new modes of failure: some interior plies become much more highly strained in the region
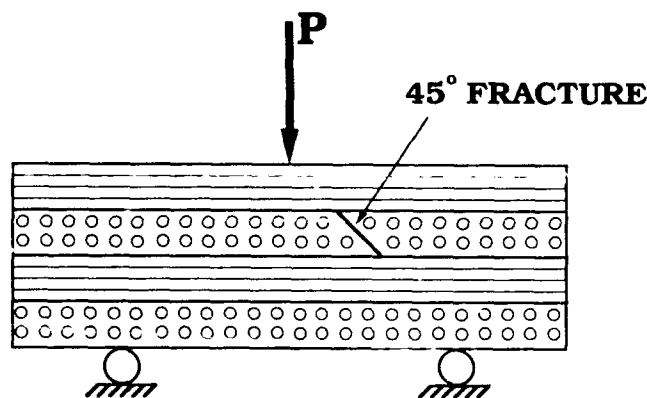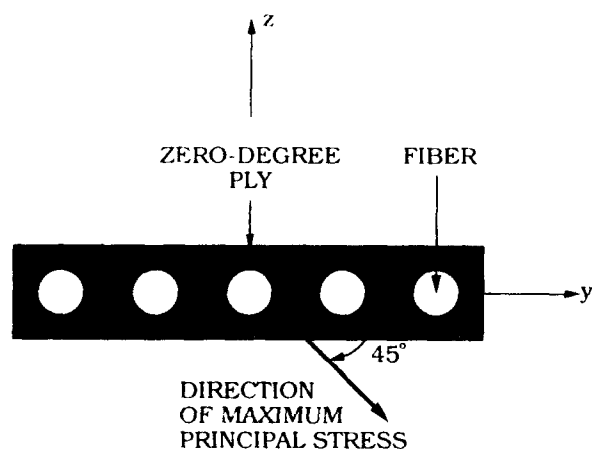
between the load nose and the support. These are 0° plies, with the new failure mode being the one shown in Fig. 15. Figures 17 and 18 show the contributions of the two individual McCleskey failure modes. In summary, Fig. 17 includes the two failure modes observed by McCleskey. By comparison with Fig. 9, the map of Fig. 16 shows a significantly increased nearness to failure in the interior of this specimen. While there is not enough of an increase to make this a principal initial failure location, the possibility of cracking in the interior of the specimen is significantly enhanced.

Strain Energy Release Rate Analysis—EAL modelling was used to construct strain energy release rate profiles at three locations. In the first profile, a crack of length 1.778 mm (0.07 in.), centered beneath the load nose, was considered. It was necessary to make the crack this length to distance the crack tip from the region of the symmetry plane used in the model. A schematic of the mesh is shown in Fig. 2 for a crack between the 45°/−45° plies at Interface 32. This crack was assumed at each of the various interfaces, and the resulting strain energy release rates were calcu-
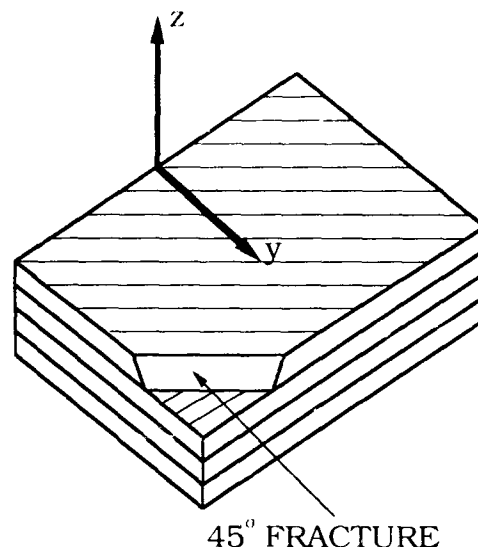

FIG. 13—*First McCleskey failure mode.*

FIG. 14—*Modelling of first McCleskey failure mode.*

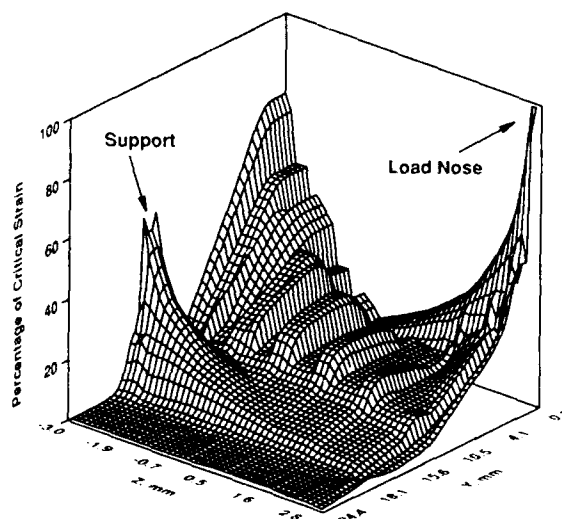FIG. 15—*The second McCleskey failure mode.*

FIG. 16—*Map of nearness to failure incorporating McCleskey failure modes.*

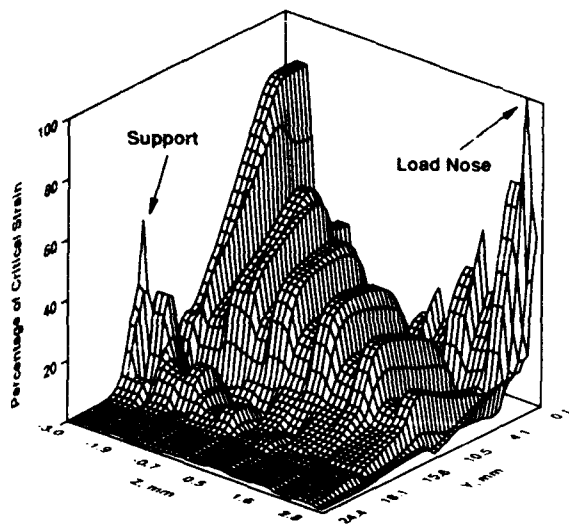FIG. 17 — Map of fraction of critical strain as a result of first McCleskey failure mode.

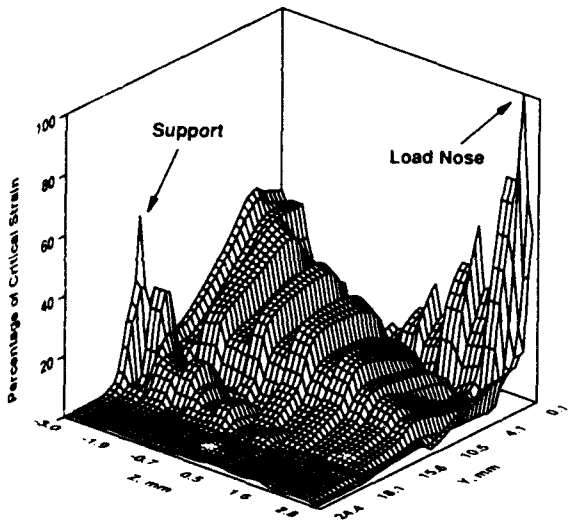FIG. 19 — Strain energy release rate data from EAL.

FIG. 18 — Map of fraction of critical strain as a result of second McCleskey failure mode.

lated. This addressed specimen behavior in the region of maximum absolute chord stress and peel stress. In the second profile, this was repeated for an assumed crack of length 0.254 mm (0.01 in.), centered 10.16 mm (0.40 in.) from the load nose, near the region of maximum absolute shear stress. Finally, a crack of length 2.54 mm (0.10 in.) was assumed at the free end, suggested by initial observation to be the site of crack initiation. The applied load in all cases was 4448 N (1000 lbs). as with the stress maps.

The profile for the assumed crack near the free end showed what Figs. 6, 7, and 8 suggest: negligible values of the strain energy release rate, too small to produce failure. The data for the first two profiles appear as Fig. 19. The distance y is as defined in Figs. 6, 7, and 8.

Note that all data points shown in Fig. 19 are taken from locations at least 1.016 mm (0.04 in.) from the surface of the specimen. Thus, for all data points, the peel stress is negligible, as indicated by Fig. 6. Consequently, crack growth is predominantly Mode II. The spikes in the G distribution result from variations in elastic properties from ply to ply.
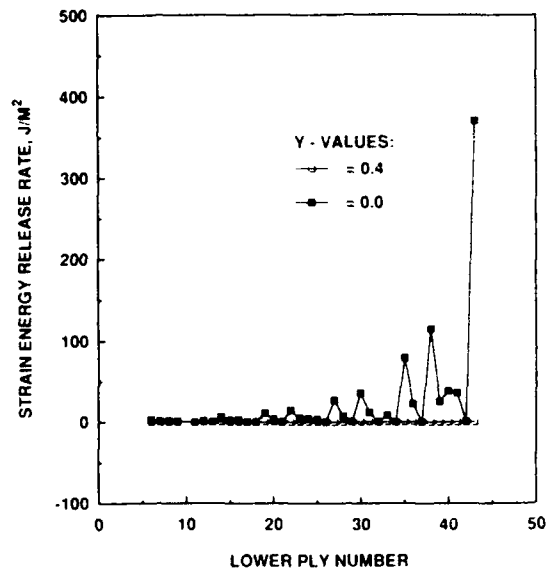
As shown in Fig. 19, the strain energy release rate for assumed interlaminar cracks beneath the load nose increases rapidly as the flaw is placed nearer to the point of application of the load. However, for flaws assumed in the range of high shear stress away from the load nose, strain energy release rates remain relatively negligible. Figure 19 shows that cracking can occur in plies near the load nose, but is unlikely away from this region. This supports the data of Fig. 9, which indicate that overstress failure is found in this same region.

Results of Fractographic Analysis

Microscopic analysis of a failed specimen showed several pertinent features, many of which were visible with the naked eye after the specimen had been sputter-coated. Directly beneath the load nose, many cracks were observed running perpendicular to the direction of load application. One such is shown in Fig. 20. This crack was approximately 6.35 mm (0.25 in.) long and was found beneath the load nose, above the midplane.

Figure 21 shows some smaller flaws in the same region. The presence of such flaws supports the analytical determination that extensive damage as a result of crushing in this region will lead to the growth of cracks.

Figure 22 shows the failure of a 45° ply below the midplane, near the load nose. This ply has experienced matrix failure, splitting in two along the fiber direction. This supports the analytical prediction of ply failure in this location as a result of chordwise stresses.

The presence of matrix failure suggests an explanation for the failure of all specimens below the midplane. In this region, the chordwise stresses are positive, leading to possible tensile failure of the matrix, which is more likely to lead to complete specimen failure than is the compressive failure which is to be found above the midplane.

Conclusion

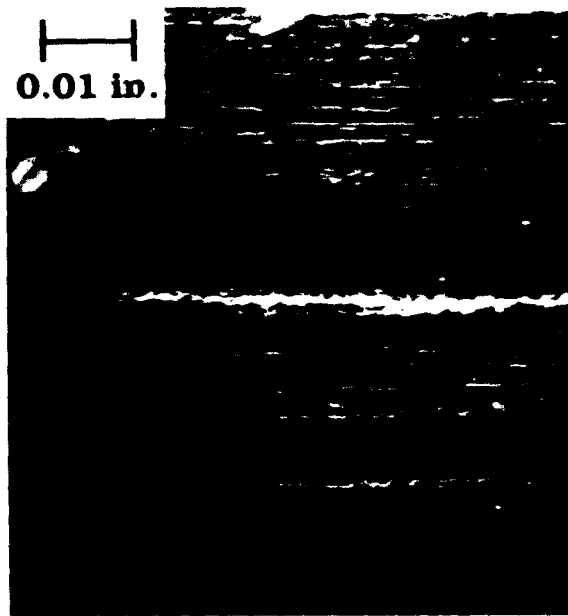Finite-element analyses have been used to describe the behavior of a quasi-isotropic short beam specimen. Short beam
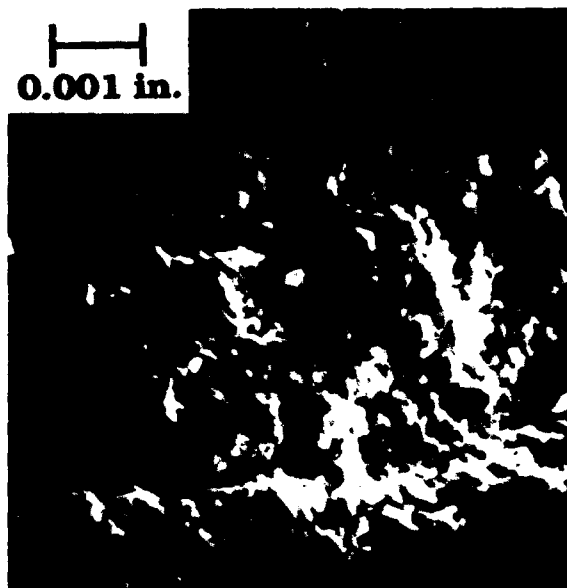
FIG. 20 — Crack beneath load nose

FIG. 22 — Matrix failure of a 45° ply

FIG. 21 — Small cracks beneath load nose

the midplane, it is caused by chordwise tensile stresses. These regions of damage are sites from which delamination cracks can propagate. Eventually, the region beneath the midplane becomes sufficiently damaged to produce a delamination that will propagate to failure. The cracks originating above the midplane are subjected to a compressive chordwise stress and to a larger compressive peel stress.

The strength of materials method neglects the chordwise and crushing loads which are the driving forces causing failure in this type of specimen. Therefore, the three-point short-beam shear test does not measure the interlaminar shear strength of a quasi-isotropic laminated composite. Because of the interaction of damage modes in this configuration, the quantitative data cannot be interpreted as a measure of a simple, isolated failure mode.

specimens have been tested and the results compared with the analyses, and the fracture surfaces of failed specimens have been examined.

Fractographic analyses show that numerous small cracks are created directly beneath the load nose, possibly causing fracture to proceed from this location. This is supported by the presence of large magnitudes of peel, shear, and chordwise stresses in the vicinity of the load nose, as shown by the FEM analysis, and by comparison of strain energy release rate values obtained at the same locations.

The following mechanism may be postulated. Stresses cause matrix failures beneath the load nose. Above the midplane, this failure is caused by crushing stresses in the z direction; below
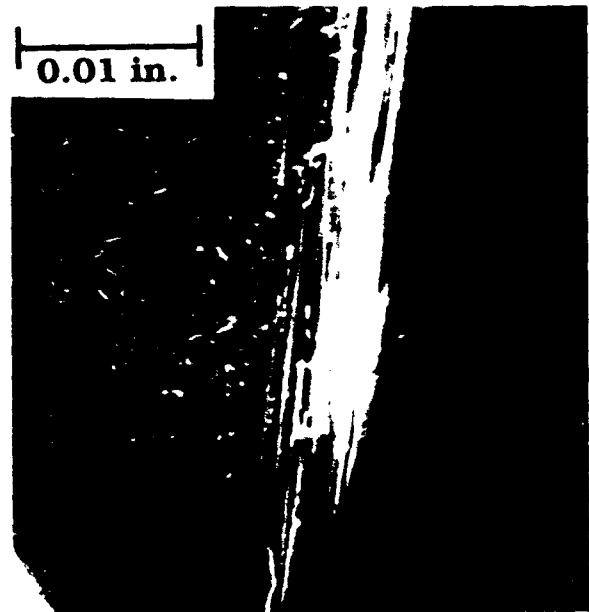
References

[1] Whitney, J. M. and Browning, C. E., "On Short-Beam Shear Tests for Composite Materials," *Experimental Mechanics*, Sept. 1985, pp. 294-300.

[2] Berg, C. A., Tirosh, J., and Israeli, M., "Analysis of Short Beam Bending of Fiber Reinforced Composites," in *Composite Materials Testing and Design (Second Conference)*, ASTM STP 497, American Society for Testing and Materials, Philadelphia, 1971, pp. 206-218.

[3] Sandorff, P. E., "Saint-Venant Effects in an Orthotropic Beam," *Journal of Composite Materials*, Vol. 22, 1980, pp. 199-212.

[4] Whitcomb, J. D. and Dattaguru, B., "User's Manual for GAMNAS Geometric and Material Nonlinear Analysis of Structures," NASA-TM-85734, Jan. 1984.

[5] Rybicki, E. F. and Kanninen, M. F., *Engineering Fracture Mechanics*, Vol. 9, 1977, pp. 931-938.